Monthly Notices
of the
ROYAL ASTRONOMICAL SOCIETY

MNRAS **475,** 3076–3082 (2018)
Advance Access publication 2018 February 2

doi:10.1093/mnras/stx3333

Observational properties of SNe Ia progenitors close to the explosion

A. Tornambé,[1] L. Piersanti,[2,3]★ G. Raimondo[2] and R. Delgrande[1,4,5]

[1]*INAF-Osservatorio Astronomico di Roma, via Frascati, 33, I-00040, Monte Porzio Catone, Italy*
[2]*INAF-Osservatorio Astronomico d'Abruzzo, via Mentore Maggini, snc, I-64100, Teramo, Italy*
[3]*INFN-Sezione di Perugia, via A. Pascoli, I-06123 Perugia, Italy*
[4]*Physics Department, Università di Roma 'Tor Vergata', via della Ricerca Scientifica, 1, I-00133, Roma, Italy*
[5]*INFN-LNF, via E. Fermi 40, I-00044, Frascati, Italy*

Accepted 2017 December 18. Received 2017 December 18; in original form 2017 July 14

ABSTRACT

We determine the expected signal in various observational bands of supernovae Ia progenitors just before the explosion by assuming the rotating double-degenerate scenario. Our results are valid also for all the evolutionary scenarios invoking rotation as the driving mechanism of the accretion process as well as the evolution up to the explosion. We find that the observational properties depend mainly on the mass of the exploding object, even if the angular momentum evolution after the end of the mass accretion phase and before the onset of C-burning plays a non-negligible role. Just before the explosion, the magnitude M_V ranges between 9 and 11 mag, while the colour (F225W − F555W) is about −1.64 mag. The photometric properties remain constant for a few decades before the explosion. During the last few months, the luminosity decreases very rapidly. The corresponding decline in the optical bands varies from a few hundredths up to one magnitude, the exact value depending on both the white dwarf total mass and the braking efficiency at the end of the mass transfer. This feature is related to the exponentially increasing energy production, which drives the formation of a convective core rapidly extending over a large part of the exploding object. Also, a drop in the angular velocity occurs. We find that observations in the soft *X* band (0.5–2 keV) may be used to check if the evolution of the SNe Ia progenitors up to the explosion is driven by rotation and, hence, to discriminate among different progenitor scenarios.

Key words: binaries: general – supernovae: general.

1 INTRODUCTION

Despite their pivotal role in observational cosmology, type Ia supernovae (SNe Ia) still remain an intriguing mystery, as there is no clear consensus for their progenitor systems. In fact, the observational properties of the resulting explosive event are largely independent of the scenario considered for the progenitor's explosion, mainly because the explosion itself smears out almost completely the previous evolutionary imprint. It has been suggested that some indications about the progenitors could be derived by analysing archival images of the site where a SN Ia explodes (e.g. Li et al. 2011; Kelly et al. 2014; McCully et al. 2014). We note that the imprint of the progenitor could be found if either the donor star is still there at the epoch of the explosion, as expected in the classical single-degenerate (SD) scenario (Whelan & Iben 1973), or some material from the donor remains in the circumstellar medium, as is possible in the classical double-degenerate (DD) scenario (Iben & Tutukov 1984).

In recent years, it has been suggested that rotation plays a major role in determining the evolution up to the explosion (Piersanti et al. 2003a,b; Di Stefano, Voss & Claeys 2011; Hachisu, Kato & Nomoto 2012). In fact, in interacting binary systems, the accretor may acquire a large rotational velocity owing to the continuous angular momentum deposition via mass transfer. Rotation overcomes many shortcomings of both the SD and DD scenarios; in addition, it represents a key ingredient in the core-degenerate (CD) scenario of Ilkov & Soker (2012). Since rotation lifts stellar structures, it transpires that rotating objects can increase their total mass above the canonical Chandrasekhar mass limit and, hence, the rotating scenarios for SNe Ia progenitors allow one to explain the origin of both normal and superluminous events, the leading parameter being the total mass of the exploding object. An important consequence of such an evolutionary scenario is that accreting white dwarfs (WDs) in the mass range 1.4–2.2 $M_\odot$ are stable,[1] as the pressure gradient is exactly counterbalanced by the effective gravity (gravitational

★ E-mail: piersanti@oa-abruzzo.inaf.it

[1] The upper limit is fixed by considering that in the DD scenario, the maximum allowed mass for a CO WD is not larger than 1.1 $M_\odot$, according to standard stellar evolution. On the other hand, in the SD scenario, due to the partial retention of the accreted matter on to the CO WD, it appears quite unrealistic that the mass of the exploding object could exceed such a limit (see also Hachisu et al. 2012).

plus centrifugal forces), so that they cannot attain the physical conditions suitable for C-ignition in the innermost zone. To get such an outcome, it is necessary that the angular velocity profile of the accreting WD is modified, either via internal angular momentum distribution, as occurs in differentially rotating objects, or via angular momentum losses. Even if the exact physical characterization of these two processes is still unknown, it is reasonable to estimate that they need at least several 10^6 yr. During this time, all the information of the original binary systems is lost, so that the only way to find *directly* an imprint of the donor star would be to analyse astronomical frames taken in the Pleistocene!

In the present work, we derive the expected observational properties of SN Ia progenitors close to the explosion epoch by assuming that rotation is the leading parameter driving both the mass transfer phase and the evolution up to carbon ignition at the centre. With this aim, we adopt the rotating DD scenario of Piersanti et al. (2003a,b) for the progenitors and we compute full evolutionary models from the onset of the mass transfer process up to the dynamical breakout, which occurs when the temperature at the burning point approaches $\sim 8 \times 10^8$ K (Lesaffre et al. 2006). We note that our analysis and findings are valid also for the rotating SD scenario as well as for the CD scenario. In fact, when rotation is properly taken into account, the mass transfer process does not directly drive the accreting WD to the explosion, but it continues up and beyond the canonical Chandrasekhar mass limit until the mass reservoir is completely exhausted. After that, the evolution up to the explosion is determined by the angular momentum redistribution alone and/or angular momentum losses from the accreted CO WD, independently of the previous evolution. Our analysis is not applicable to the *prompt merging* scenario of Pakmor et al. (2012) or to the canonical non-rotating SD scenario.

The present work is structured as follows. In Section 2, we review the accretion phase in the rotating DD scenario, exploring the dependence of the results on various assumptions about the physical mechanism driving the mass accretion process. In Section 3, we discuss the physical properties of the WD after the mass accretion has stopped and we analyse its evolution up to the explosion. In Section 4, we derive the expected observational properties during the last few months before the explosion of the massive WD. Finally, our results are summarized and discussed in Section 5.

2 THE MASS TRANSFER PHASE

In the present computations, we use as initial CO WD the same model with total mass $M_{\rm WD} = 0.8\,{\rm M}_\odot$ as in Piersanti et al. (2003a) and we assume that it is embedded in a close binary system with another CO WD with mass $M_{\rm donor} = 0.71\,{\rm M}_\odot$. We compute all the evolutionary sequences using the FRANEC evolutionary code of Chieffi & Straniero (1989), modified according to the prescriptions in Piersanti et al. (2003a,b) to account for the effects of rotation under the hypothesis for the high efficiency of angular momentum transport.

Due to the emission of gravitational wave radiation (GWR), the binary system shrinks and the less massive component first overfills its own Roche lobe, giving rise to a dynamical mass transfer so that it is completely disrupted. It forms a thick accretion disc around the surviving companion. CO-rich matter flows from the disc to the WD at a very high rate, depositing also angular momentum. The rapid mass accretion produces a huge thermal energy excess and a large increase of the surface angular velocity, so that the accretor expands in a very short time and attains the critical angular velocity at its surface. In this condition, no more matter can be added, so that

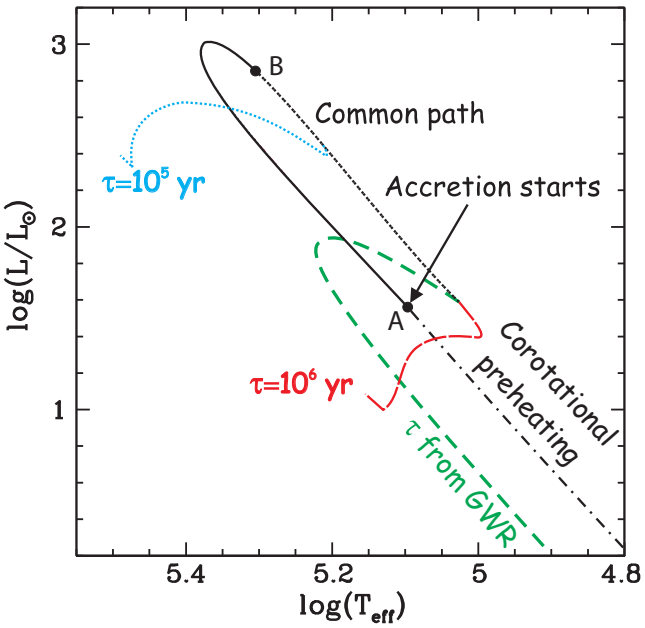

Figure 1. Evolution in the HR diagram of a $0.8\,{\rm M}_\odot$ rotating CO WD accreting mass from an accretion disc. The computation was halted when the WD attains the Chandrasekhar mass limit for rigidly rotating objects. Point A marks the onset of mass transfer, while point B is the epoch when the critical angular velocity is attained on the surface of the accretor. The dotted line is the model computed by assuming for the braking time-scale $\tau_{\rm B} = 10^5$ yr, while the sequence depicted with a long dashed line was obtained by fixing $\tau_{\rm B} = 10^6$ yr. For comparison, we plot also the model computed by Piersanti et al. (2003b), under the assumption that angular momentum is lost via GWR after the accretor has deformed into a Jacobi ellipsoid (heavy dashed line).

mass deposition stops for a while and, hence, the thermal energy can diffuse inward and the WD can contract. The accretor recedes from the critical conditions and mass deposition can resume. The rate at which matter can be added to a CO WD is determined by its structural properties, in particular by the temperature profile. Later, when the structure becomes thermally balanced, so that the inward heat transfer time-scale becomes longer, the effective accretion rate is determined by other physical mechanisms. Piersanti et al. (2003b) showed that owing to the continuous deposition of angular momentum, the rotational energy of the WD increases and when this attains a critical value, the accretor adopts an ellipsoidal shape, so that it acquires a quadrupole momentum. GWR is emitted, thus braking down the WD itself. Several different mechanisms have been suggested by various authors to describe the angular momentum losses from an accreting WD (see e.g. Andersson, Kokkotas & Stergioulas 1999; Ilkov & Soker 2012; Boshkayev et al. 2014, and references therein). In the present work, we do not assume any specific physical mechanism, but we describe such a process as an exponential law by adopting two characteristic time-scales, namely $\tau_{\rm B} = 10^5$ and 10^6 yr, as representative of the braking efficiency.[2]

In Fig. 1, we report the evolution in the Hertzsprung–Russell (HR) diagram of the models computed with different braking time-scales, as labelled. For comparison, we report also the model computed by assuming that angular momentum is lost from the accreting WD via GWR emission, as discussed in detail in Tornambé &

[2] The formulation of the braking law is the same as in Piersanti et al. (2003b). See their equation (3) and the corresponding discussion in section 4.

Piersanti (2013). In the figure, we display only the evolution relative to the accretion phase, i.e. up to when the total mass stored in the accretion disc has been transferred to the CO WD and its total mass approaches the Chandrasekhar mass limit for rigidly rotating degenerate objects.

Fig. 1 clearly illustrates that the surface properties of the accreting WD do depend on the angular momentum evolution, as determined by both the mass deposition and the efficiency of the physical mechanism decreasing the angular momentum. In particular, independently of the assumed value for τ_B, after the onset of the self-regulated accretion phase at point A, all the models follow the same evolutionary path, which is determined only by the inward diffusion of the thermal energy excess produced on the surface by mass deposition during the early phase of mass transfer (from point A to B in Fig. 1).

During the self-regulated accretion phase, the mass transfer rate progressively decreases as the thermal balance along the accreting WD is approached and the evolutionary time-scale becomes longer. The following evolution and, hence, the luminosity at which the accretor starts contracting and evolves blueward depend on the assumed braking efficiency. In particular, the higher τ_B, the larger the braking efficiency, the higher the corresponding mass (and angular momentum) deposition rate and, hence, the higher the luminosity. Fig. 1 also shows that for the model having braking efficiency determined by the GWR emission, the luminosity of the accretor drops rapidly during the last part of the mass transfer phase, when its total mass approaches the Chandrasekhar mass limit for rigidly rotating degenerate objects. In fact, according to the discussion in section 3.3 of Piersanti et al. (2003b), the GWR efficiency drops rapidly, thus determining a rapid reduction of the effective mass transfer rate. As a consequence, the thermal imbalance in the accretor is completely smeared out by thermal diffusion active on a time-scale shorter than 10^7 yr, so that the surface luminosity rapidly decreases. The model with $\tau_B = 10^6$ yr exhibits a moderate decrease of the surface luminosity, while that with $\tau_B = 10^5$ yr maintains almost the same luminosity. According to the previous considerations, in models with high braking efficiencies, the thermal energy delivered in the surface layers during the early phase of mass transfer remains locally stored up to the end of the mass deposition phase. This has an important consequence for the expected observational properties during the following evolutionary phase, when the WD attains the physical conditions for carbon ignition in the inner zone where the degeneracy level is very high (see Section 3).

We emphasize here that the accretion process ceases once the total mass of the smaller WD has been accreted on to the larger WD, leaving no circumstellar material to veil the surface of the remaining WD prior to its explosion.

We note that our results do not depend on the initial mass of the accreting WD, as discussed in Tornambé & Piersanti (2013, see their fig. 5), because at each epoch, the evolutionary properties depend only on the assumed efficiency of angular momentum losses, for a fixed value of the total mass of the accretor.

The results discussed above have been obtained assuming high efficiency of angular momentum transport inside the accreting WD, so that the accretor behaves as a rigid rotator. However, the same considerations and results are still valid also when assuming that the angular momentum transport inside the CO WD is a secular process, albeit with some relevant differences. First, due to the local storage of the deposited angular momentum in the external layers, the accreting WD attains the critical conditions more rapidly. Moreover, as the spinning-up decreases the effective local gravity, the density in the external layers is lower with respect to rigidly rotating degenerate objects and, hence, the compressibility of the zone is higher. As a consequence, when angular momentum transport is treated as a secular process, the surface layers of the accretor heat up at a higher rate, so, as a whole, the evolution in the HR diagram is quite similar to those displayed in Fig. 1 (from A to B), even if the exact luminosity level as well as the corresponding effective temperature at the epoch of the Roche instability (point B in Fig. 1) depends on the efficiency of angular momentum transport. During the self-regulated accretion phase, since a large part of the deposited angular momentum remains localized in the surface layers, the effective mass accretion rate decreases more rapidly with respect to rigidly rotating objects. As a consequence, the evolutionary time-scale becomes longer and, hence, angular momentum can be transferred inward efficiently. In fact, the luminosity at which the accretor starts evolving blueward is determined by the interplay between angular momentum losses and inward angular momentum transport, which, in turn, determines the exact value of the effective mass accretion rate. According to the previous considerations, we can safely derive that, independently of the angular momentum transport efficiency, a differential rotating WD attains a lower luminosity for a fixed value of the efficiency of angular momentum losses. Finally, since the effective mass transfer rate is lower and, hence, the evolutionary time-scale is longer, the thermal energy excess in the external layers is smeared out very rapidly, like for a rigid rotating model losing angular momentum via GWR. The luminosity drop, displayed in Fig. 1 for the latter model, could not occur at all because the differential rotating WD could never reach its own Chandrasekhar mass limit[3] during the mass and angular momentum deposition phase.

3 THE FINAL PATH TO THE EXPLOSION

In the rotating DD scenario, all the available mass constituting the original donor and forming the accretion disc around the accreting CO WD is completely transferred without causing C-ignition, and, hence, an explosion as a SN Ia. In fact, rotation decreases the effective gravity along the whole structure, so that strong gravitational contraction as the total mass increases is avoided. Therefore, when the mass reservoir has been exhausted, the resulting object is a stable massive WD, whose further evolution should be a slow and continuous cooling. However, it has been suggested that these massive rotating objects are secularly unstable and, hence, they should lose angular momentum via different physical mechanisms (see e.g. Andersson et al. 1999; Ilkov & Soker 2012; Boshkayev et al. 2014, and references therein). Owing to the reduction of the total angular momentum, the WD undergoes strong compression, so that it can heat up and ignite carbon in the innermost zones in highly degenerate physical conditions.

To model this phase, once again we adopt an exponentially decaying law for the total angular momentum and we parametrize the efficiency of angular momentum losses by using a different time-scale, as in the previous section. In Fig. 2, we report the evolution in the HR diagram of models computed by adopting $\tau_B = 10^5$ yr and different total masses of the initial binary system, as labelled, from the end of the mass transfer process up to the explosion epoch (marked with a dot).

Notice that, as already recognized (Geroyannis & Papasotiriou 2000; Boshkayev et al. 2013), when angular momentum is removed

[3] Recall that, depending on the angular velocity profile, the Chandrasekhar mass limit for a differentially rotating degenerate object can exceed 5 $M_\odot$.

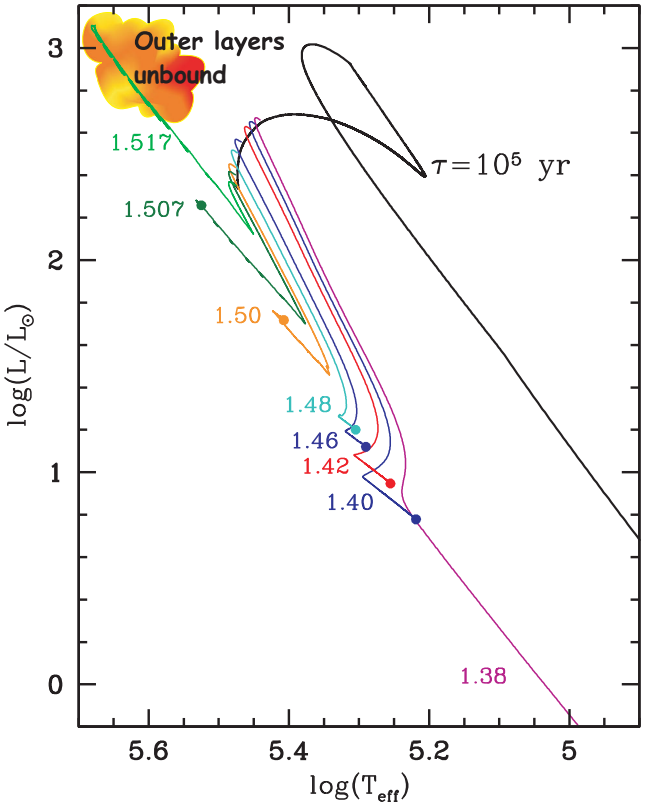

Figure 2. Evolution in the HR diagram of models with different total mass M_F, as labelled, and the same efficiency of angular momentum losses. The evolution refers to the time spanning from the end of the mass transfer process and the epoch of the explosion, marked with a heavy dot.

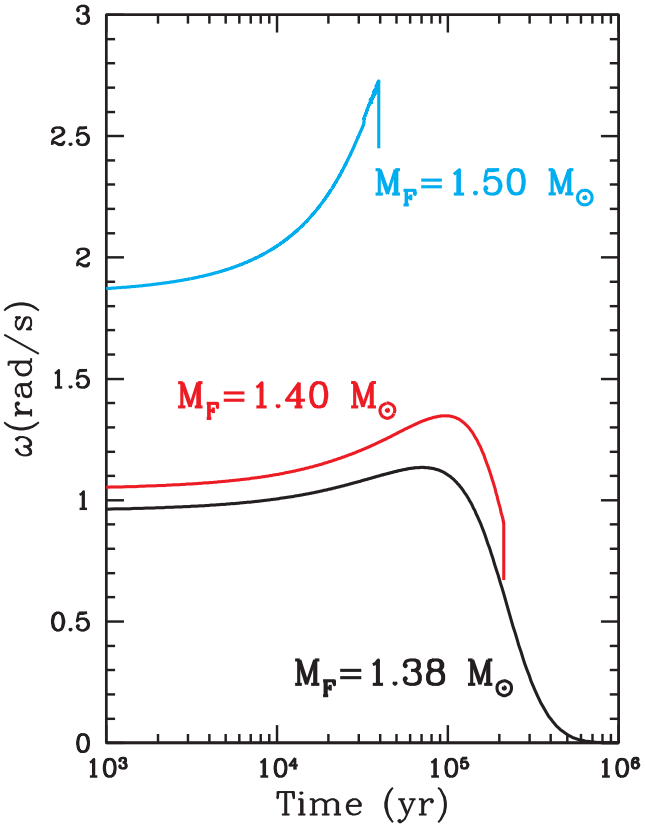

Figure 3. Time evolution of the angular velocity ω for models with different total masses (as labelled), but the same efficiency of angular momentum losses. The time is set arbitrarily to zero at the epoch of the end of the mass transfer process.

from a rigidly rotating degenerate object more massive than the canonical non-rotating Chandrasekhar mass limit, the structure reacts by increasing its rotational velocity. This is clearly shown in Fig. 3, where we report the time evolution of the angular velocity for models losing angular momentum with $\tau_B = 10^5$ yr and different total masses, as labelled. Such behaviour can be easily understood when considering that rotating stars are not solid but gaseous. As a consequence, when angular momentum is subtracted, the local effective gravity increases and the star reacts by contracting to achieve a new hydrostatic equilibrium and, hence, spins up. In fact, all the models considered in Fig. 2 experience an increase of the angular velocity as angular momentum is lost. In any case, the critical angular velocity on the surface increases more rapidly than ω, so that the structure is gravitationally stable.

As angular momentum continues to be subtracted, WDs with different total mass experience different evolutionary paths. In particular, the model with $M_F = 1.38\,M_\odot$ becomes fully supported by the pressure of degenerate electrons and, hence, cannot contract further. Thus, the angular momentum losses remain the only physical process driving the evolution of the angular velocity, which attains a maximum and later decreases continuously until the WD is practically at rest. Models more massive than $1.39\,M_\odot$ but smaller than $1.42\,M_\odot$ experience the same evolution even if, owing to the homologous compression of the whole structure, they succeed in igniting carbon before the large part of the star attains highly degenerate physical conditions (see the model with $M_F = 1.40\,M_\odot$ in Fig. 2). Finally, massive WDs contract so rapidly and, hence, heat up so efficiently, that carbon is ignited when the star is still spinning up. The drop in the angular velocity after the accretion process observed in the final part of the curves corresponding to models with total mass $M_F = 1.40$ and $1.50\,M_\odot$ is due to the onset of central convection triggered by the huge energy released via $^{12}C + {}^{12}C$ reactions.

The evolution of surface properties of the considered models after the end of the accretion process and up to the explosion depends mainly on the actual total mass of the accreted WD. In particular, after the mass reservoir is exhausted and the evolution of the WD is driven by the angular momentum loss, all the computed models experience a luminosity drop (see Fig. 2). In this phase, owing to the reduction of angular momentum, the accreted WD contracts, heating up via homologous compression. In addition, as the evolutionary time-scale becomes longer, the thermal energy excess in the accreted layers determined by the local compression via mass deposition is efficiently removed via inward thermal diffusion, while plasma neutrino emission efficiently reduces the thermal content of the whole star.[4] In models with total mass lower than $1.50\,M_\odot$, the thermal diffusion occurs on a time-scale shorter than the compressional heating determined by the angular momentum losses, so that the decrease of the surface luminosity continues up to when $^{12}C + {}^{12}C$ reactions are fully ignited (corresponding to the point with the largest effective temperature in Fig. 2). At variance, for larger masses, the luminosity starts to increase before C-burning is ignited at a significant level. This different behaviour is because more massive WDs are closer to the rotating Chandrasekhar mass limit. As a

[4] Radiative losses are almost negligible in this phase

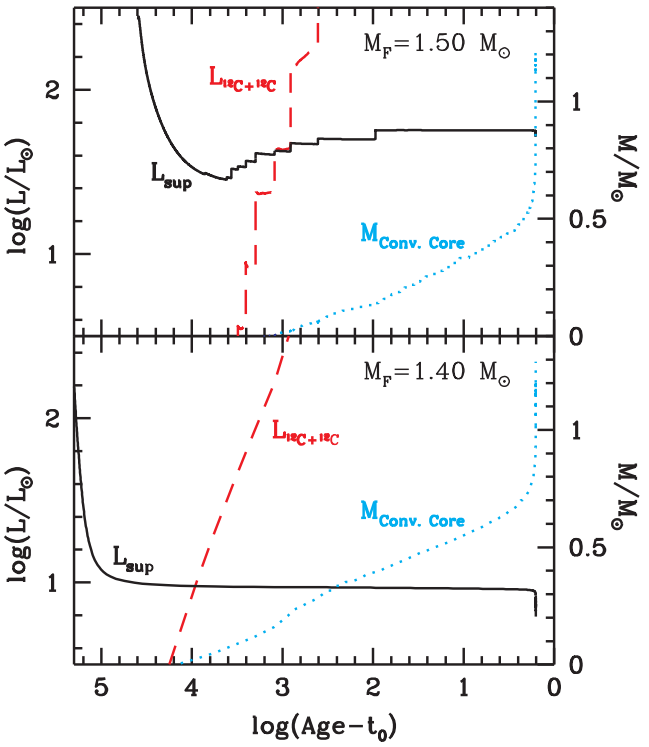

Figure 4. Temporal evolution of the surface luminosity (solid line), the carbon-burning luminosity (dashed line) and the mass extension of the convective core (dotted line) for models with total mass $M_F = 1.40$ and $1.50\,M_\odot$ (lower and upper panels, respectively). Time (in years) is expressed relative to the epoch of the explosion, which has been set to $t_0 = 2.1198 \times 10^5$ and 3.9245×10^4 yr for models in the lower and upper panels, respectively. For both models, we assume that angular momentum losses occur on the same time-scale, namely $\tau_B = 10^5$ yr.

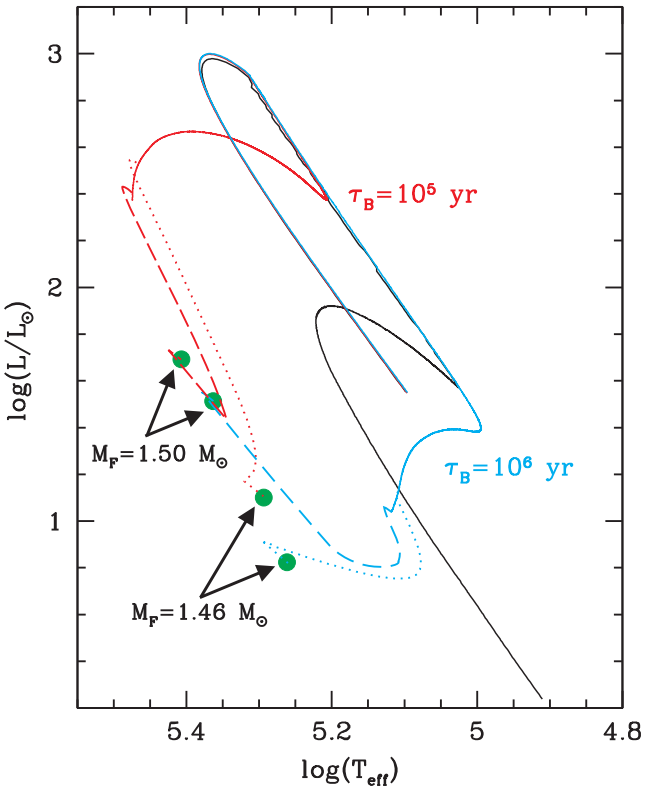

Figure 5. Evolution in the HR diagram of models with different total masses and efficiencies of angular momentum losses.

consequence, the contraction driven by angular momentum losses triggers a more rapid and, hence, more efficient compressional heating of the whole star, thus determining an increase of the surface luminosity.

This is illustrated in Fig. 4, where we report results for models with total mass after accretion $M = 1.40$ and $1.50\,M_\odot$ (lower and upper panels, respectively). The figure shows the total surface luminosity ($L_{\rm sup}$, solid lines), the luminosity produced by carbon fusion reactions ($L_{^{12}C+^{12}C}$, dashed lines) and the mass extension of the convective core ($M_{\rm Conv.Core}$, dotted lines). Fig. 4 also shows that the energy (per unit of time) produced via carbon burning at the centre very quickly triggers the formation of a convective zone, which rapidly grows in mass, involving almost 95 per cent of the whole star. This determines a new change in the physical properties of the star, which starts to expand since the thermal content in the whole convective region largely deviates from that of a cold fully degenerate object. As a consequence, the star expands and, hence, as the evolutionary time-scale becomes shorter than the time-scale on which angular momentum is removed, the angular velocity starts to decrease (see the sudden drop in the ω profiles for models with total mass $M_F = 1.40$ and $1.50\,M_\odot$ in Fig. 3). This corresponds to the last few days of evolution before the explosion.

In Fig. 5, we compare the evolution in the HR diagram of models with the same total mass, namely $1.46\,M_\odot$ (dotted lines) and $1.50\,M_\odot$ (dashed lines), but with different efficiencies of angular momentum losses after the end of the mass transfer phase. We note that, for a fixed value of the total mass, the surface properties of the exploding objects are quite similar, independently of the time-scale adopted to remove angular momentum. This finding is confirmed by several other computations performed by varying both M_F and τ_B.

Finally, we note that during the last part of the evolution, when the WD starts to expand due to the large energy injected by C-burning, both ω and the critical angular velocity on the surface decrease, but at a different rate, so that the star remains gravitationally bound. The only model deviating from this behaviour is the one with total mass $M_F = 1.517\,M_\odot$. In this case, the most external layers experience the Roche instability so that it can be argued that $\sim 0.01\,M_\odot$ of matter has to be lost before the explosion can occur.

4 THE OBSERVATIONAL PROPERTIES

To compare theoretical models with the observational properties of SN Ia progenitors, we assume genuine blackbodies as well as spectral energy distribution models. To our knowledge, carbon and oxygen model atmospheres of such peculiar WDs do not exist in the extant literature, so we adopt pure-helium models from the library available in the Tubingen non-local thermodynamic equilibrium (NLTE) Model-Atmosphere Package (TMAP) data base[5] (Rauch & Deetjen 2003; Rauch 2010).

Table 1 lists the theoretical and the corresponding observable values for the set of rotating SN Ia progenitors considered in the present work at the epoch of the explosion. We provide, for each model, the mass and luminosity (columns 1 and 2, solar units), the

[5] http://astro.uni-tuebingen.de/∼rauch/

Table 1. Expected AB absolute magnitudes in various bands for SN Ia progenitors just before explosion based on blackbody models. The different masses of the models considered are determined by the rotationally driven accretion mechanism, as suggested by Piersanti et al. (2003b). Lines 1–7 refer to models computed by adopting as braking time-scale 10^5 yr and displayed in Fig. 2, while lines 8 and 9 are models computed with braking time-scale 10^6 yr and displayed in Fig. 5.

Mass ($M_\odot$)	$\log(L/L_\odot)$	$\log(T_{\rm eff})$	FUV	NUV	*u*	*g*	*r*	*i*	*z*	F435W	F814W	0.5–2 keV	2–10 keV
						$\tau_B = 10^5$ yr							
1.400	0.77	5.22	8.14	8.87	9.78	10.33	10.92	11.32	11.70	10.18	11.48	1.67E+23	6.34E-25
1.420	0.94	5.26	7.98	8.73	9.64	10.20	10.78	11.19	11.57	10.04	11.34	3.91E+24	3.59E-19
1.460	1.11	5.29	7.76	8.51	9.43	10.00	10.58	10.99	11.36	9.83	11.14	3.87E+25	3.79E-15
1.480	1.19	5.31	7.70	8.45	9.38	9.94	10.53	10.94	11.31	9.78	11.09	1.52E+26	1.20E-12
1.490	1.26	5.32	7.59	8.35	9.27	9.84	10.42	10.84	11.21	9.68	10.99	3.17E+26	2.07E-11
1.500	1.71	5.41	7.09	7.87	8.80	9.37	9.96	10.38	10.75	9.21	10.53	8.28E+28	1.29E-01
1.507	2.25	5.52	6.52	7.31	8.26	8.83	9.43	9.84	10.22	8.67	10.00	2.03E+31	4.37E+08
						$\tau_B = 10^6$ yr							
1.460	0.83	5.26	8.26	9.00	9.91	10.47	11.06	11.47	11.84	10.32	11.62	3.04E+24	2.79E-19
1.500	1.53	5.36	7.19	7.96	8.89	9.45	10.04	10.50	10.83	9.30	10.60	5.04E+27	9.73E-07

effective temperature (column 3, in K), absolute AB magnitudes for the *GALEX* filters FUV and NUV (columns 4 and 5, respectively), the Sloan filters (columns 6–10), two filters of the Advanced Camera for Surveys (ACS) on board the *Hubble Space Telescope* (*HST*), and, finally, the luminosity in two X-ray bands.

We perform the same evaluation by considering NLTE model atmospheres. Synthetic magnitudes in the *GALEX*, Sloan and ACS photometric bands, as well as for filters in the UVIS and IR channels of the Wide Field Camera 3 (WFC3) have been calculated using the IRAF task CALCPHOT of STSDAS and calibrated with WDs in the *HST* data base.[6] A selection of magnitudes is reported in Table 2. As can be easily noticed, pure He models are 0.3–0.5 mag fainter than blackbody models, the exact value depending on the mass of the exploding object and on the adopted braking efficiency.

The values listed in Tables 1 and 2 span the whole range of expected magnitudes for SN Ia progenitors close to the explosion in the rotationally driven scenario discussed in the previous sections. We emphasize again that the results are independent of the assumed scenario for the progenitors (SD, DD and CD scenarios) since they are determined mainly by the total mass of the exploding object and, to a lesser extent, on the physical mechanism driving the braking and/or the angular momentum redistribution during the accretion phase. Inspection of these two tables reveals that the spectral distribution peaks in the far-UV/soft-X range. Moreover, they also show that the related optical emission would be so weak that only nearby events would be detectable.

5 DISCUSSION AND FINAL REMARKS

The recent observations of SN 2011fe in M101 (Nugent et al. 2011a,b) and SN 2014J in M82 (Fossey et al. 2014; Zheng et al. 2014) have stimulated a large debate about the possibility of constraining observationally their progenitor systems.

Several studies have reported observational features and suggested possible progenitor systems (e.g. Li et al. 2011; Kelly et al. 2014; McCully et al. 2014). Observations at different wavelengths have suggested that some progenitor systems associated with the SD scenario have to be ruled out for SN 2011fe, leaving a very limited phase space compatible with the DD scenario and really exotic SD systems (Li et al. 2011; Chomiuk et al. 2012). Optical nebular spectra do not show any evidence for narrow H α emission, supporting again a degenerate companion for SN 2011fe. A pre-explosion frame in the *HST* archive exhibits the same properties, so that red giants and most helium-star companions can be safely ruled out (Li et al. 2011). By using pre-explosive archival *HST* images of M82 from the near-UV to the near-IR, Kelly et al. (2014) excluded for SN 2014J a progenitor system having a bright red giant donor, including recurrent novae with luminosities comparable to the Galactic prototype symbiotic system RS Oph. According to the available data, these authors also remark that a system consisting of two CO WDs as well as a system comprising a CO WD and a main sequence star cannot be excluded.

In the rotationally driven scenario described in the previous sections, it is not surprising that even for nearby SN 2011fe and SN 2014J, the imprint of the progenitor system cannot be detected in archival frames. In this regard, we note that the SN 2011fe progenitor should have a magnitude in the ACS/F435W band of ∼38 mag or higher, while the current observational limit is 27.4 mag (Li et al. 2011). Also, the largest possible X-ray emission in the 0.5–2 keV band, corresponding to the model with mass 1.507 $M_\odot$ (see Table 1), is several orders of magnitude lower than the upper limit inferred for SN 2014J by Nielsen et al. (2014). In fact, only SN Ia progenitors in our own Galaxy may be detectable.

As a final consideration, we note that, according to predictions in Tables 1 and 2, models accounting for the effects of rotation exhibit a strong feature in the 0.5–2 keV band, having an expected flux that depends on the total mass of the progenitor. Such a feature is completely missing in standard non-rotating Chandrasekhar mass models of SNe Ia owing to their lower effective temperature. This is clearly illustrated in Fig. 6, where we compare models with $\tau_B = 10^5$ yr and different total masses with the ZSUN model in Piersanti et al. (2017), obtained by directly accreting CO-rich matter on to an initial 0.817 $M_\odot$ CO WD at $\dot{M} = 10^{-7}$ $M_\odot$ yr^{-1}, mimicking the evolution of a SD system. For the latter object, the expected flux in the 0.5–2 keV band mass is vanishingly small whereas it becomes appreciable for the more massive models obtained in the rotationally driven scenario. As a consequence, it seems that the X-ray flux, even if small, can be used to assess the role played by rotation in the evolution of SN Ia progenitors.

[6] ftp://ftp.stsci.edu/cdbs/currentcalspec/

Table 2. AB magnitudes for selected filters as derived from NLTE atmospheres models.

Mass ($M_\odot$)	V	FUV	NUV	u	g	r	i	z	F225W	F336W	F475W	F555W	F814W	F110W
						$\tau_B = 10^5$ yr								
1.400	11.00	8.40	9.17	10.10	10.66	11.25	11.65	12.03	9.26	9.98	10.69	10.90	11.78	12.51
1.420	10.87	8.27	9.05	10.00	10.54	11.12	11.53	11.90	9.14	9.86	10.57	10.78	11.66	12.38
1.460	10.68	8.08	8.85	9.78	10.35	10.93	11.34	11.71	8.95	9.67	10.38	10.59	11.46	12.18
1.480	10.64	8.04	8.81	9.74	10.31	10.89	11.30	11.67	8.91	9.63	10.34	10.55	11.42	12.14
1.490	10.55	7.94	8.72	9.65	10.21	10.80	11.20	11.57	8.81	9.54	10.24	10.46	11.33	12.05
1.500	10.14	7.54	8.32	9.25	9.81	10.39	10.80	11.16	8.41	9.13	9.84	10.05	10.92	11.64
1.507	9.65	7.04	7.82	8.76	9.32	9.90	10.30	10.67	7.91	8.64	9.35	9.56	10.43	11.14
						$\tau_B = 10^6$ yr								
1.460	11.15	8.55	9.33	10.25	10.82	11.40	11.81	12.18	9.42	10.14	10.85	11.06	11.94	12.66
1.500	10.19	7.59	8.37	9.30	9.86	10.44	10.85	11.22	8.46	9.18	9.89	10.10	10.98	11.70

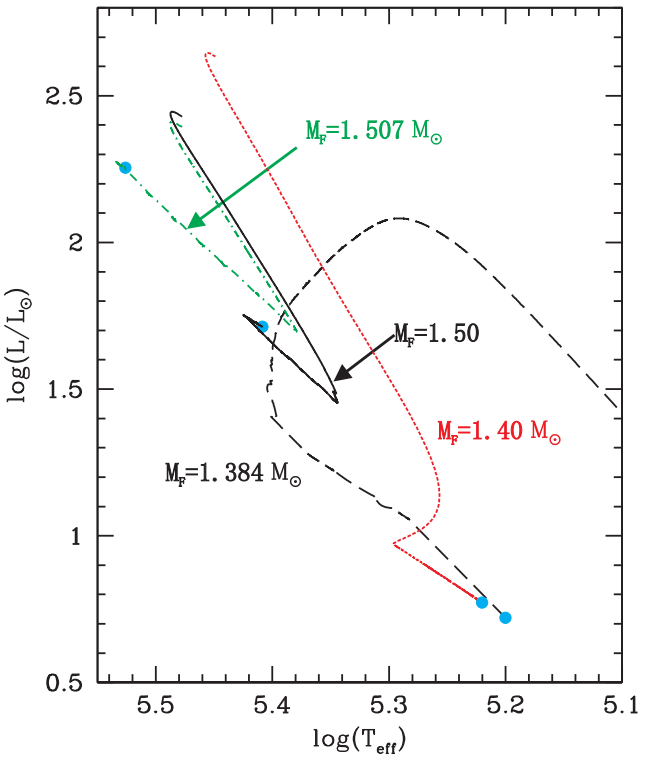

Figure 6. Comparison between a classical non-rotating standard model arising in a SD binary system (long dashed line, $M_{\rm F} = 1.384\,{\rm M}_\odot$) and selected models reported in Fig. 2, with $\tau_B = 10^5$ yr and different masses, as labelled.

ACKNOWLEDGEMENTS

It is a pleasure to thank several colleagues for their advice and comments, including I. Domínguez, C. Badenes, B. Fisher, E. Cappellaro, M. Turatto, J. Isern, S. Benetti, E. Bravo, F. Mannucci, M. Dall'Ora, M. Della Valle and E. Garcia-Berro. We also want to thank the referee, J. Danziger, for his useful comments and suggestions, which improved the presentation of our results. This work received partial financial support from INAF-PRIN/2014 (principal investigator Clementini). The TheoSSA service (http://dc.g-vo.org/theossa), which was used to retrieve the theoretical spectra in this work, was constructed as part of the activities of the German Astrophysical Virtual Observatory.

REFERENCES

Andersson N., Kokkotas K. D., Stergioulas N., 1999, ApJ, 516, 307
Boshkayev K., Rueda J. A., Ruffini R., Siutsou I., 2013, ApJ, 762, 117
Boshkayev K., Rueda J. A., Ruffini R., Siutsou I., 2014, J. Korean Phys. Soc., 65, 855
Chieffi A., Straniero O., 1989, ApJS, 71, 47
Chomiuk L. et al., 2012, ApJ, 750, 164
Di Stefano R., Voss R., Claeys J. S. W., 2011, ApJ, 738, L1
Fossey S. J., Cooke B., Pollack G., Wilde M., Wright T., 2014, Cent. Bureau Electron. Telegrams, 3792
Geroyannis V. S., Papasotiriou P. J., 2000, ApJ, 534, 359
Hachisu I., Kato M., Nomoto K., 2012, ApJ, 756, L4
Iben I., Jr, Tutukov A. V., 1984, ApJS, 54, 335
Ilkov M., Soker N., 2012, MNRAS, 419, 1695
Kelly P. L. et al., 2014, ApJ, 790, 3
Lesaffre P., Han Z., Tout C. A., Podsiadlowski P., Martin R. G., 2006, MNRAS, 368, 187
Li W. et al., 2011, Nature, 480, 348
McCully C. et al., 2014, Nature, 512, 54
Nielsen M. T. B., Gilfanov M., Bogdán Á., Woods T. E., Nelemans G., 2014, MNRAS, 442, 3400
Nugent P. E. et al., 2011a, Nature, 480, 344
Nugent P., Sullivan M., Bersier D., Howell D. A., Thomas R., James P., 2011b, Astron. Telegram, 3581
Pakmor R., Kromer M., Taubenberger S., Sim S. A., Röpke F. K., Hillebrandt W., 2012, ApJ, 747, L10
Piersanti L., Gagliardi S., Iben I., Jr, Tornambé A., 2003a, ApJ, 583, 885
Piersanti L., Gagliardi S., Iben I., Jr, Tornambé A., 2003b, ApJ, 598, 1229
Piersanti L., Bravo E., Cristallo S., Domínguez I., Straniero O., Tornambé A., Martínez-Pinedo G., 2017, ApJ, 836, L9
Rauch T., 2010, TheoSSA TMAP Web Interface, VO resource provided by the GAVO Data Center. Available at: http://dc.zah.uni-heidelberg.de/theossa/q/web/info
Rauch T., Deetjen J. L., 2003, in Hubeny I., Mihalas D., Werner K., eds, ASP Conf. Ser. Vol. 288, Stellar Atmosphere Modeling. Astron. Soc. Pac., San Francisco, p. 103
Tornambé A., Piersanti L., 2013, MNRAS, 431, 1812
Whelan J., Iben I., Jr, 1973, ApJ, 186, 1007
Zheng W. et al., 2014, ApJ, 783, L24

This paper has been typeset from a TEX/LATEX file prepared by the author.